The Relationship between Winds, Surface Roughness, and Radar Backscatter at Low Incidence Angles from TRMM Precipitation Radar Measurements

MICHAEL H. FREILICH AND BARRY A. VANHOFF

College of Oceanic and Atmospheric Sciences, Oregon State University, Corvallis, Oregon

ABSTRACT

One year of collocated, rain-free normalized backscatter cross-section measurements from the Tropical Rainfall Mapping Mission (TRMM) precipitation radar (PR) and wind speed estimates from the TRMM Microwave Imager are used to construct fully empirical model functions relating cross section to wind speed for incidence angles from 0° (nadir) to 18°. With the exception of a ~1.9-dB offset, the TRMM PR model function at nadir compares well with TOPEX and *Geosat* results. For the first time using spaceborne data, least squares fits of the TRMM PR model functions to the geometric optics scattering formulation allow direct solution for the magnitudes and wind speed dependencies of Ku-band effective nadir reflectivity and effective mean square slope [$s(u)$]. Effective reflectivity is found to decrease slightly with increasing wind speed above 3.5 m s^{-1}. A logarithmic dependence of $s(u)$ is found for wind speeds between 1 and 10 m s^{-1}. Both linear and two-branch logarithmic dependencies (with a slope break at 10 m s^{-1}) are excellent and statistically indistinguishable parameterizations for $s(u)$ for wind speeds between 5 and 19 m s^{-1}. Calculations using the Elfouhaily et al. wave model suggest that the effective Ku-band $s(u)$ corresponds to a cutoff wavelength of 3 to 6 times the radar wavelength for wind speeds from 5 to 25 m s^{-1}; at lower wind speeds, the cutoff wavelength increases rapidly consistent with earlier observations.

1. Introduction

Spaceborne estimation of ocean surface winds using active microwave instruments is based on the variation of normalized radar cross section (σ_0) as a function of local wind conditions and observation geometry. Accurate theoretical specification of the relationship between σ_0 and winds is hindered by uncertainties regarding both the processes causing electromagnetic scattering from a realistically rough ocean surface (cf. reviews by Brown 1990; Plant 1990 and references therein), and the detailed connection between winds and centimeter-scale sea surface roughness (Apel 1994; Elfouhaily et al. 1997). Operational estimation of winds from satellite-borne active radar instruments has thus relied on substantially empirical "model functions" relating σ_0 to wind conditions and measurement geometry [see Chelton et al. (2001) for a review of wind speed model functions for nadir altimeters, and Wentz et al. (1984) and Wentz and Smith (1999) for empirical vector wind model functions for Ku-band scatterometers]. This study uses radar measurements from the Tropical Rainfall Mapping Mission (TRMM) to quantitatively examine aspects of low-incidence angle scattering mechanisms and the relationship between surface roughness and wind speed.

Quasi-specular reflection is thought to dominate microwave scattering at small (near-vertical) incidence angles, and simple analytic formulations relating σ_0 to near-nadir surface roughness and surface dielectric properties have been derived (Barrick 1974; Holliday et al. 1986; Brown 1990; and many others). The two key parameters in the simple models are the nadir reflection coefficient and a quantity related to the mean square slope of the sea surface. Although some of the assumptions required to derive the simple models are clearly violated under realistic ocean conditions, the functional forms of the approximate analytic formulations are remarkably accurate—quantitatively correct σ_0 values can be calculated by specifying empirically determined values for "effective" reflectivity and "effective" wind-speed-dependent mean square slope. Owing to a lack of microwave measurements to date obtained from small, but nonzero incidence angles, it has not previously been possible to use spaceborne data to investigate details of the empirical effective reflectivity and mean square slope.

The launch and successful operation of the Tropical Rainfall Mapping Mission (Kummerow et al. 1998, 2000) has provided a unique, long-term, extensive dataset of accurate wind speed measurements from the passive TRMM Microwave Imager (TMI) and Ku-band

Corresponding author address: Michael H. Freilich, College of Oceanic and Atmospheric Sciences, Oregon State University, 104 Ocean Admin. Building, Corvallis, OR 97331-5503.
E-mail: mhf@coas.oregonstate.edu

σ_0 data from the TRMM precipitation radar (PR). Since the PR measurement swath falls entirely within the broader radiometer swath, TMI wind speed estimates are available for all PR σ_0 measurements. As importantly, the PR measurement scheme results in σ_0 measurements with high spatial resolution over a range of incidence angles from nadir (0°) to 18°. The PR measurements thus fully cover the incidence angle regime in which quasi-specular scattering processes dominate. At the outer portions of the PR swath, the data extend into the transition region where resonant scattering from tilted, rough facets becomes significant (Donelan and Pierson 1987; Plant 1990; Apel 1994, and references therein).

The present study uses TRMM spaceborne radar data to examine details of effective reflectivity and effective roughness, in order to quantify aspects of both near-nadir scattering processes and the relationship between wind conditions and surface mean square slope. Fully empirical model functions relating 13.8-GHz PR σ_0 to near-surface wind speed as a function of incidence angle are first derived from collocated TMI and PR measurements. The model functions in turn are analyzed in light of dynamically based scattering and surface roughness models. The incidence angle range covered by the PR measurements allows, for the first time, the use of spaceborne data for direct and separate calculation of effective ocean surface reflectivity and effective mean square slope. The wave model of Elfouhaily et al. (1997) is combined with the calculated effective mean square slopes to estimate the wind speed dependence of the high wavenumber cutoff for Ku-band altimeters, thus allowing more precise interpretation of the empirical, effective mean square slope values.

The present work represents an extension of the pioneering study of Jackson et al. (1992). Whereas they analyzed a dataset acquired by a broad-swath airborne radar altimeter under a limited range of wind conditions at a few sites, this investigation benefits from the large geographical coverage and wide range of synoptic conditions measured by TRMM. In addition, the present study makes use of recent advances in the modeling of wind-driven surface roughness.

The PR and TMI datasets used in the study are presented in section 2. Section 3 describes the derivation of fully empirical model functions relating PR σ_0 to wind speed for all incidence angles covered by the PR measurement swath. The empirical model functions are analyzed in light of quasi-specular scattering theory to determine the magnitudes and wind speed dependencies of effective reflectivity and effective mean square slope in section 4; this section also contains the analysis of effective cutoff wavenumbers for Ku-band altimeters based on the PR effective mean square slope solutions and the surface wave model of Elfouhaily et al. (1997). A summary and conclusions are presented in section 5.

2. Datasets

The Tropical Rainfall Measuring Mission was launched on 27 November 1997 into a 350-km altitude, inclined ($\pm 35°$ latitude) orbit. The primary TRMM scientific objectives centered on remote measurement of precipitation using passive and active microwave instruments, as well as a visible and infrared radiometer. Details of the mission, spacecraft, instrument suite, and initial on-orbit performance and validation are given in Kummerow et al. (1998, 2000) and the extensive references therein. Our focus in the proposed investigation is on secondary geophysical wind speed information derived from the two microwave instruments—the active TRMM precipitation radar and the passive TRMM Microwave Imager.

TRMM was maintained in its 350-km orbit from 1997 through August 2001. Station-keeping fuel was depleted relatively rapidly at this low altitude, especially as the initial mission period coincided with the solar maximum. In August 2001, the TRMM orbit was raised to conserve the remaining fuel and increase the useful mission lifetime. The orbit raising maneuver introduced a discontinuity in the mission data record; at the higher altitude, the spatial resolutions of the TMI and PR instruments degraded, and swath widths changed. The dataset descriptions and the analyses performed for this investigation are limited to the 1-yr period August 1999 through July 2000, during which TRMM was in the lower orbit.

a. TRMM precipitation radar (PR)

The PR is the first spaceborne precipitation radar. It was designed to measure the vertical distribution of rainfall over both land and ocean. The PR data thus complement the passive microwave measurements from TMI and visible/IR data from the TRMM Visible and Infrared Scanner (VIRS) instrument. Descriptions of the PR instrument design and operation are found in Kozu et al. (2001), Kummerow et al. (1998, 2000), and Meneghini et al. (2000). This section emphasizes the characteristics and capabilities of the instrument and standard data products that relate specifically to the measurement of the ocean surface σ_0. Algorithms for deriving σ_0 from the PR have received significant attention in the TRMM program, since knowledge of the surface cross section is critical for estimating total path attenuation and thus rain rate (cf. Meneghini et al. 2000).

The PR radar operates at 13.8 GHz, transmitting and receiving horizontally polarized radiation. The PR is the first spaceborne broad-swath radar capable of measuring ocean radar backscatter at relatively low incidence angles over a significant swath width and with high spatial resolution. Classical altimeters, such as TOPEX/Poseidon, are operated to acquire high quality backscatter cross-section measurements only within about 1° of nadir, while the *Seasat-A* scatterometer measured near-

nadir σ_0 only at 0°, 4°, and 8° incidence angles (Grantham et al. 1977). The PR radar uses an active phased-array antenna system to make measurements in each of 49 cross-track bins as the satellite orbits. Adjacent cross-track bins are separated by about 0.75° in incidence angle, corresponding to a spatial resolution of ~4.3 km. Although the scan angle of the PR beam (measured relative to the local vertical at the satellite) ranges from 0° to 17° on each side of the subsatellite point, the incidence angle (measured relative to the local vertical at the mean sea surface) ranges from 0° to 18°, owing to the large-scale curvature of the earth. Adjacent measurements are separated by about 4.2 km in the along-track dimension. The full PR measurement swath is ~215 km wide, with continuous surface backscatter cross-section measurements having spatial resolution of ~4.3 km.

The PR 2A21 standard product (Kummerow et al. 2000; Meneghini et al. 2000) forms the basis for the results presented here. It contains information on ocean surface radar backscatter cross section, total path attenuation, and the presence of rain in the measurement cell, as well as standard quality flags and navigation and instrument geometry (e.g., incidence angle) information. The 2A21 data products for the period August 1999 through July 2000 were obtained from the Goddard Distributed Active Archive Center. Only PR surface cross-section measurements obtained under rain-free conditions were used for this study.

The PR instrument was intensively calibrated and validated through comparisons with an Active Radar Calibrator located at a site in Japan, with an expected absolute accuracy of <1 dB; continued instrument monitoring using both internal and external (ground comparison) techniques indicated that the receiver and transmitter gains remained stable to within about ±0.2 dB (Kummerow et al. 2000). However, as discussed in section 3, comparisons between PR and historical altimeter data suggest a mean discrepancy of ~2 dB in absolute calibration between the PR and previous spaceborne altimeters.

b. TRMM Microwave Imager (TMI)

The TRMM Microwave Imager is a multichannel, broad-swath, conically scanning passive multifrequency microwave radiometer. Instrument design, operation, and calibration details are given in Kummerow et al. (1998, 2000) and Wentz et al. (2001). While based on the operational Special Sensor Microwave Imager (SSM/I) instruments on the Defense Meteorological Satellite Program spacecraft, the TMI includes several design changes and enhancements. The nominal TMI incidence angle was changed to 52.75° (vs 53.4° for SSM/I). The TMI water vapor line measurement was moved to 21.3 GHz (vs 22.235 for SSM/I) to reduce saturation at the low inclination of the TRMM orbit. Finally, in addition to acquiring data near all of the SSM/I frequencies, the TMI measures vertically and horizontally polarized brightness temperatures at 10.7 GHz.

At the low altitude of the TRMM orbit, the TMI effective field of view (along-track, cross-track) ranges from about (63, 37 km) for the 10.7-GHz channels to about (16, 9 km) at 37 GHz. By coordinating the TMI antenna rotation rate of 31.6 rpm with the TRMM ground track speed of 6.9 km s^{-1}, a total contiguous TMI measurement swath of ~759 km is achieved. The swath is centered on the subsatellite track, and thus includes and extends well beyond the 215-km-wide PR swath.

The TMI brightness temperatures prior to the TRMM orbit raising in August 2001 have been comprehensively calibrated and validated (Wentz et al. 2001). Their validation process used a comprehensive suite of statistical analyses to identify and eliminate systematic cross-track (scan position) effects, and included calibration based on comparisons with collocated SSM/I data, and analysis of TMI measurements obtained while the spacecraft was temporarily oriented to view deep space (Wentz et al. 2001).

Significant processing is required to extract surface wind speed estimates from the multifrequency TMI antenna temperature measurements (Wentz 1997; Wentz and Spencer 1998); however, wind speeds based on microwave radiometer measurements are routinely produced to an accuracy of ~1.5 m s^{-1} (Mears et al. 2001; Meissner et al. 2001) and preliminary validation with buoy comparisons yield TMI wind speed accuracies of ~0.84 m s^{-1} [www.ssmi.com; also see Connor and Chang (2000) for an analysis of TMI wind speeds derived using an alternate set of algorithms]. This study uses version 3 of the in-swath TMI wind speeds based on 11-GHz brightness temperature measurements, quality flags, and rain data obtained from the Remote Sensing Systems archives (available online at www.ssmi.com). These data are posted on a 0.25° grid separately for ascending and descending swaths, and wind speeds are provided with 0.20 m s^{-1} precision.

c. Collocation and editing of PR and TMI data

The TMI swath fully overlaps the PR swath (Fig. 1), greatly simplifying the collocation process and resulting in negligible temporal and spatial location differences between the measurements from the two instruments. For this study, contemporaneous TMI wind speeds were bilinearly interpolated in space to the location of each nonraining PR σ_0 measurement. To ensure the highest quality comparison wind data, an interpolated TMI–PR pair was only produced if the four closest, nonraining TMI wind estimates were all within 25 km of the PR location. Since the TMI data from Remote Sensing Systems are posted on a 0.25° grid, this constraint required that a PR measurement be surrounded by contiguous nonraining TMI data in order for it to be included in the collocated dataset. The collocation and editing pro-
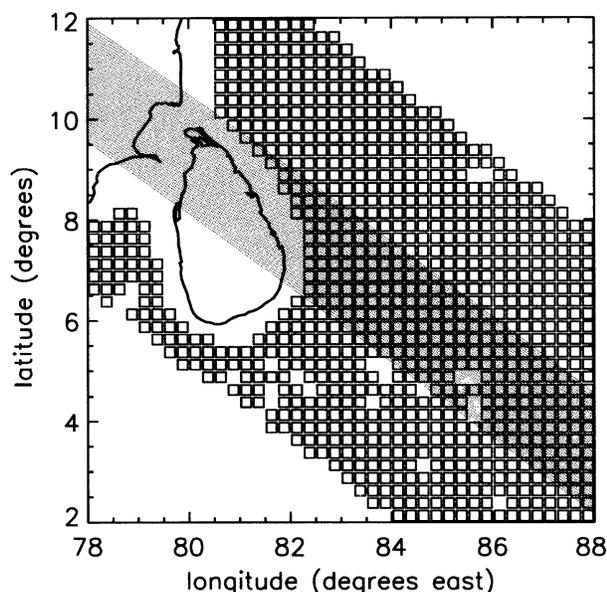
FIG. 1. Measurement locations for the TRMM PR (small dotted gray swath) and TMI (0.25° squares) from a short segment of TRMM orbit 9729 (6 Aug 1999) near the island nation of Sri Lanka. Missing data result from land masking of the TMI measurements and elimination of rain-contaminated measurements from both instruments.
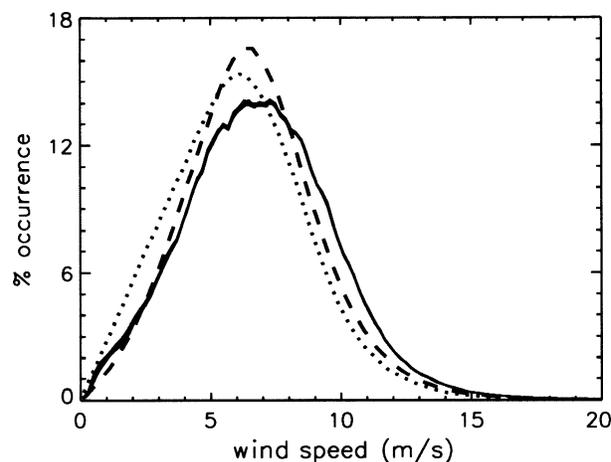

FIG. 2. Histograms of collocated wind speed measurements. Solid lines: collocated TMI speeds at each PR incidence angle. Dashed line: interpolated NCEP 10-m speeds. Dotted line: interpolated ECMWF 10-m speeds.

cedure applied to the 12 months of data analyzed here yielded more than 1.1×10^7 TMI wind speed and PR σ_0 pairs at each PR incidence angle.

Histograms of interpolated TMI wind speeds at each PR incidence angle are shown in Fig. 2. As expected, the annual sample distributions of wind speed did not differ significantly as a function of PR cross-swath location, although the wind conditions at any instant could vary significantly within the PR swath.

Also shown in Fig. 2 are histograms of 10-m wind speeds based on operational $1° \times 1° \times 6$-hourly surface analyses from the National Centers for Environmental Prediction (NCEP) and the European Centre for Medium-Range Weather Forecasts (ECMWF), trilinearly interpolated to the space–time locations of nonraining PR measurements. Differences exist between the NCEP and ECMWF histograms, and between the histograms based on either of the operational analyses and that calculated from TMI measurements. The TMI and NCEP distributions have similar means (6.8 and 6.6 m s^{-1} for TMI and NCEP, respectively) and standard deviations (2.8 and 2.6 m s^{-1}); the ECMWF winds have a lower mean (6.2 m s^{-1}) and a larger standard deviation (3.5 m s^{-1}).

3. Empirical model functions for low incidence angles

Altimeters designed to measure sea surface elevation also measure backscatter at near-vertical incidence angles (i.e., $\theta \ll 1°$), while scatterometers make measurements at moderate incidence angles ($17° \lesssim \theta \lesssim 65°$)

where σ_0 is sensitive to both wind speed and wind direction. It is thus not surprising that virtually all previous empirical model function efforts have focused on these nadir and moderate incidence angle regimes, to the exclusion of the incidence angle range $1° \lesssim \theta \lesssim 17°$. In this section, fully empirical model functions relating σ_0 at low incidence angles to winds are developed using the edited, rain-free, collocated PR and TMI datasets described in section 2 above.

a. General approach and results

Most published approaches for determining empirical scatterometer model functions at moderate incidence angles utilize multiple, collocated σ_0 measurements obtained from different azimuthal viewing geometries (e.g., Stoffelen and Anderson 1997; Wentz and Smith 1999); indeed, such azimuthally diverse measurements form the core of spaceborne wind scatterometry (e.g., Naderi et al. 1991). These techniques cannot be used in the case of the TRMM PR, since measurements at only a single azimuth are available at each location within the PR swath, and the TMI data do not provide information on wind direction.

Freilich and Dunbar (1993) developed a fully empirical approach for the development of altimeter model functions, based on analyses of measured mean σ_0 at each incidence angle in narrow wind speed bins. This "conditional mean" approach requires only that the σ_0 and collocated wind measurements have small random error; they performed simulations to quantify the sensitivity of the empirical nadir model function to random errors in the wind speed data used to bin the backscatter measurements.

In this study, we follow the Freilich and Dunbar (1993) approach assuming that the measured σ_0 at all incidence angles within the PR swath depends only on
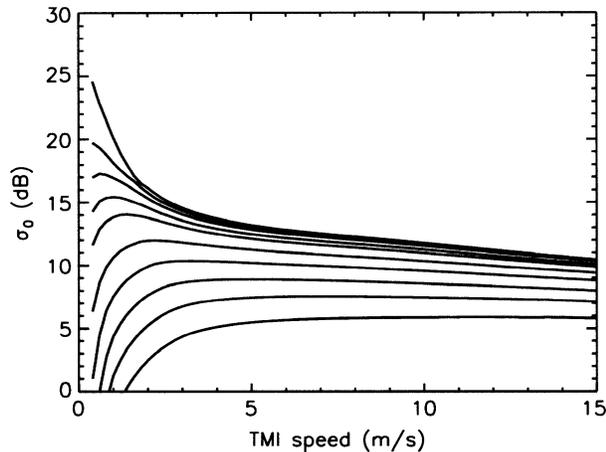
FIG. 3. Fully empirical PR model functions at selected incidence angles. From top to bottom: $\theta = 0.1°$, $2.2°$, $2.9°$, $3.7°$, $4.4°$, $5.9°$, $7.4°$, $8.9°$, $10.4°$, and $11.9°$.
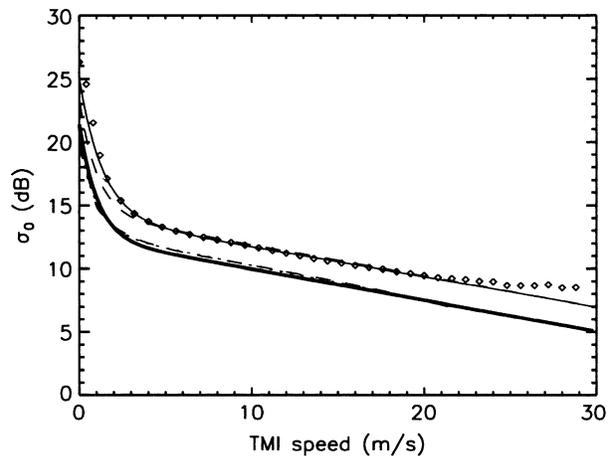

FIG. 4. Comparison of empirical nadir model functions. Diamonds: raw PR model function from the present analysis. Heavy solid line: Freilich and Challenor model function. Heavy dashed line: MCW model function. Light dotted line: best fit to the MCW model function using the Freilich and Challenor ad hoc parameterization (1). Light solid: best fit to the raw PR model function using (1). Light dashed: Freilich and Challenor model function offset by 1.92 dB. Best-fit model coefficients are given in Table 1.

wind speed (wind directional effects are neglected; Li et al. 2002). The collocated TMI wind speed estimates therefore suffice for binning the PR σ_0 data. At each PR incidence angle, all collocated, rain-free σ_0 and wind speed data were assigned to 0.20 m s^{-1} bins based on the interpolated TMI wind speeds. A 3σ filter was applied iteratively to convergence in each wind speed and incidence angle bin to eliminate "outlier" σ_0 measurements, which result from either contaminated PR σ_0 measurements or inaccurate TMI wind speeds. The empirical, tabular model function, denoted by $\hat{\sigma}_0(u; \theta)$, is formed from the sample mean σ_0 in each wind speed and incidence angle bin (calculated from the outlier-removed data in natural, not dB, units).

Empirical model functions at selected incidence angles are shown in Fig. 3. Near nadir ($\theta = 0.1°$), the approach yields the well-known monotonically decreasing function of σ_0 with increasing wind speed. In the range $2° \lesssim \theta \lesssim 10°$, σ_0 first increases, then decreases with increasing wind speed (see section 4 below). Backscatter cross section is nearly insensitive to wind speed near $\theta \approx 11°$ for wind speeds $\gtrsim 4$ m s^{-1}, and σ_0 becomes a monotonically increasing function of wind speed for $\theta \gtrsim 11°$ (Wentz et al. 1984; Apel 1994; Li et al. 2002).

The standard deviations of the edited σ_0 measurements in each wind speed and incidence angle bin were also calculated (not shown). For all incidence angles and wind speeds exceeding ~ 3.5 m s^{-1}, the standard deviations were less than 20% of the mean σ_0 in each bin. At lower wind speeds, bin standard deviations increased with decreasing wind speed, reaching values of $\sim 60\%$ of the mean at ~ 1.5 m s^{-1}. Variations in edited σ_0 data within a bin result from inherent noise in the radar measurements, misbinning owing to errors in the collocated TMI measurement, and variations of the true σ_0 within the finite wind speed and incidence angle ranges defined by the bin. At very low wind speeds, both TMI errors and the high sensitivity of σ_0 to wind speed contribute to increased uncertainty in the calculated mean σ_0.

b. Comparisons with altimeter-based nadir model functions and PR calibration

Many previous investigations have focused on the altimeter model function relating Ku-band σ_0 to wind speed for $\theta = 0°$ [see Chelton et al. (2001) for a comprehensive review]. Comparisons between these historical altimeter model functions and the present PR-based model for $\theta = 0°$ provide a sensitive, if indirect, calibration of the PR and TMI data. Figure 4 compares the empirical PR-based nadir model function with the Modified Chelton–Wentz (MCW) model used for TOPEX processing (Witter and Chelton 1991) and the *Geosat*-based "FC" model function (Freilich and Challenor 1994). The MCW and FC models are quantitatively similar, and the PR model has nearly the same shape. However, the PR cross sections are significantly larger than those from the *Geosat* and TOPEX altimeters at all wind speeds.

Freilich and Challenor (1994) presented an ad hoc but accurate analytic parameterization for empirical nadir model functions. They suggested that the wind speed dependence of σ_0 (in dB) could be modeled as the sum of an exponential (important at low wind speeds) and a linear decrease (dominant at moderate-to-high wind speeds) as in

$$_{dB}\hat{\sigma}_0(u; \theta = 0) = A_0 + A_1 u + A_2 \exp\{A_3 u\}, \quad (1)$$

where u denotes the neutral stability wind at 10-m height, and the explicit leading "dB" subscript highlights that $_{dB}\hat{\sigma}_0$ has units of decibels. Coefficients re-

TABLE 1. Coefficients from the ad hoc parameterization (1) for various nadir model functions.

Model function	A_0	A_1	A_2	A_3	Line type (Fig. 4)
FC (Freilich and Challenor 1994)	12.40	-0.2459	8.956	-0.9593	Thick solid
MCW (Witter and Chelton 1991)	12.94	-0.2710	7.079	-1.029	Thin dotted
PR (present study)	14.08	-0.2375	10.92	-0.7371	Thin solid
FC + 1.92 dB	14.32	-0.2459	8.956	-0.9593	Thin dashed

sulting from unweighted nonlinear least squares fits of the empirical MCW, FC, and PR model functions to (1) over the wind speed range $1.5 \le u \le 20$ m s^{-1} are listed in Table 1.

As shown by the thin solid line in Fig. 4, the ad hoc form of (1) accurately matches the nadir PR model function from 1.5 to $\sim$22 m s^{-1}. At lower wind speeds, the parameterization does not increase as rapidly as the PR model function with decreasing wind speed. For $u >$ 22 m s^{-1}, the PR model function decreases less rapidly with increasing wind speed than predicted by the parameterization. This is consistent with the results of Freilich and Dunbar (1993), who demonstrated by simulation that random errors in the wind speed measurements used for binning cause low apparent sensitivity of σ_0 to winds at high wind speeds.

The thin dashed line in Fig. 4 represents the FC model function offset by 1.92 dB at all wind speeds. The close correlation between this curve and the empirical PR nadir model function confirms that the major difference between the historical altimeter model functions and the present PR nadir result is a 1.92-dB σ_0 offset. The offset may represent a net calibration difference between the historical missions and the PR. This large discrepancy is surprising, since the on-orbit PR calibration using the ground-based Active Radar Calibrator system should be accurate to better than 1 dB (Kummerow et al. 2000; Kozu et al. 2001). However, in contrast to ocean altimeters, weather radars are not designed to observe scattering from a nearly flat, fixed surface. Caylor et al. (1997) show that errors arising from insufficient digital sampling of the returned weather radar pulse can lead to substantial underprediction biases for nadir surface σ_0. Although the PR was designed with a gate spacing of half the pulse width, sampling errors are still expected to bias PR σ_0 estimates low by $\lesssim$0.75 dB (Caylor et al. 1997).

The online documentation for the TRMM PR 2A21 surface σ_0 product (available online at http://trmm.gsfc.gov/2a21.html) notes that a 2.5-dB additive correction was made to the raw calculated PR σ_0 values to account for logarithmic averaging loss. It is beyond the scope of the present study to elucidate the details of the PR and historical altimeter low-level processing algorithms. Nonetheless, if historical altimeters did not correct for logarithmic averaging losses and if the PR sampling errors introduce a 0.75-dB low bias into the raw PR σ_0 estimates, the net difference (2.5–0.75 = 1.75 dB) could account for virtually the entire observed

offset between nadir PR and historical altimeter measurements.

4. Empirical scattering and roughness coefficients

The model functions derived in the previous section are fully empirical; no dynamical or theoretical constraints were placed on the table entries for $\hat{\sigma}_0(u; \theta)$. They thus provide a compact and statistically stable representation for the large PR–TMI collocated dataset, and the fully empirical model functions can be used to interpret and test theoretical scattering models and dynamically based models for surface roughness.

a. Analytic scattering model

Analytic models for microwave backscatter for small incidence angles have been reviewed and analyzed recently by Brown (1990) and Apel (1994). The dominant near-nadir scattering mechanism is quasi-specular reflection from nearly flat regions of the sea surface ("facets") oriented perpendicular to the incident microwave radiation. The magnitude of the scattered signal is proportional to the fraction of appropriately oriented facets on the illuminated portion of the sea surface (Cox and Munk 1954; Barrick 1974; Brown 1990; and many others). Notationally, if $p_s(\xi_x, \xi_y)$ denotes the joint probability density of the slopes of facets in two orthogonal horizontal directions, then $p_s(-\tan\theta, 0)$ corresponds to the fraction of facets oriented perpendicular to the line connecting the observer and the surface. Assuming that the source and receiver are collocated and far from the surface, the backscatter cross section is then given by

$$\sigma_0(\theta) = \pi |R(0)|^2 (\sec^4\theta) p_s(-\tan\theta, 0), \qquad (2)$$

where σ_0 is the normalized cross section in natural (not dB) units, θ is the incidence angle previously defined, and $|R(0)|^2$ is an effective nadir reflection coefficient (discussed in more detail below). The formulation (2) can be obtained from the basic Kirchoff equations in several different ways, each using a different set of assumptions (Brown 1990). It is thought to be accurate for microwave scattering from the ocean for $0 \le \theta \lesssim$ 15° (Barrick 1974; Valenzuela 1978; Holliday et al. 1986; Donelan and Pierson 1987; Brown 1990). In the limit of a Gaussian, isotropic sea surface slope distribution, (2) becomes

$$\sigma_o(u;\,\theta) = \frac{|R(0)|^2}{s(u)}(\sec^4\theta)\,\exp\left[-\frac{\tan^2\theta}{s(u)}\right], \qquad (3)$$

where $s(u)$ is a measure of the effective mean square slope (Brown 1990, and references therein). Although the assumption of isotropic, Gaussian slopes is not completely accurate (e.g., Donelan and Pierson 1987; Jackson et al. 1992; Apel 1994), the effects of anisotropy (Wentz et al. 1984) and non-Gaussianity (Jackson et al. 1992) are small and are often neglected at the small incidence angles for which (2) and (3) are consistent.

The form of (3) is qualitatively consistent with the fully empirical PR model functions illustrated in Fig. 3. For $\theta = 0°$, (3) predicts that σ_0 will be a monotonically decreasing function of u as long as $s(u)$ increases monotonically with u [assuming weak wind speed dependence of $|R(0)|^2$]. Differentiation of (3) with respect to u [neglecting terms of order $(\partial|R(0)|^2/\partial u)$] yields

$$\frac{\partial\sigma_0}{\partial u} = \frac{|R(0)|^2(\sec^4\theta)}{s^2(u)}\left[\frac{\tan^2(\theta)}{s(u)} - 1\right]\exp\left[-\frac{\tan^2(\theta)}{s(u)}\right]\frac{ds}{du}. \tag{4}$$

For $ds/du > 0$ and $\theta \neq 0$, σ_0 has a maximum at the wind speed u_{max} given by the root of

$$\tan^2(\theta) = s(u_{max}) \tag{5}$$

(Wentz et al. 1984). As noted previously, the maxima are evident in Fig. 3 for $\theta \gtrsim 2.2°$.

Inherent in the derivation of (2) and (3) is the assumption that surface curvature is small on scales comparable to and shorter than the radar wavelength (Brown 1990, and references therein). If this assumption is correct for (centimetric) Ku-band scattering from the ocean, $|R(0)|^2$ and $s(u)$ in (3) would be given by the nadir Fresnel reflection coefficient and the surface mean square slope, respectively. The assumption is certainly invalid for the wind-roughened ocean, where significant sea surface roughness with shorter scales than the centimeter wavelength of the incident microwave radiation is present. Nonetheless, Jackson et al. (1992; see also Schroeder et al. 1984; Wentz et al. 1984) as well as the present study find that the incidence angle dependence in (3) is apparently accurate, as long as the terms $|R(0)|^2$ and $s(u)$ are interpreted as *effective* reflectivity and *effective* mean square slope. The magnitudes and wind speed dependences of Ku-band effective $|R(0)|^2$ and effective $s(u)$ must thus be quantified to allow proper interpretation of the spaceborne σ_0 measurements.

b. Coefficient determination approach

The empirical model functions $\hat{\sigma}_0(u;\,\theta)$ (e.g., Fig. 3) summarize the observed variations of backscatter cross section with wind speed and incidence angle. Quasi-specular scattering theory (3) relates backscatter cross section to effective nadir reflectivity [$|R(0)|^2$], effective mean square slope [$s(u)$], and incidence angle (θ). The
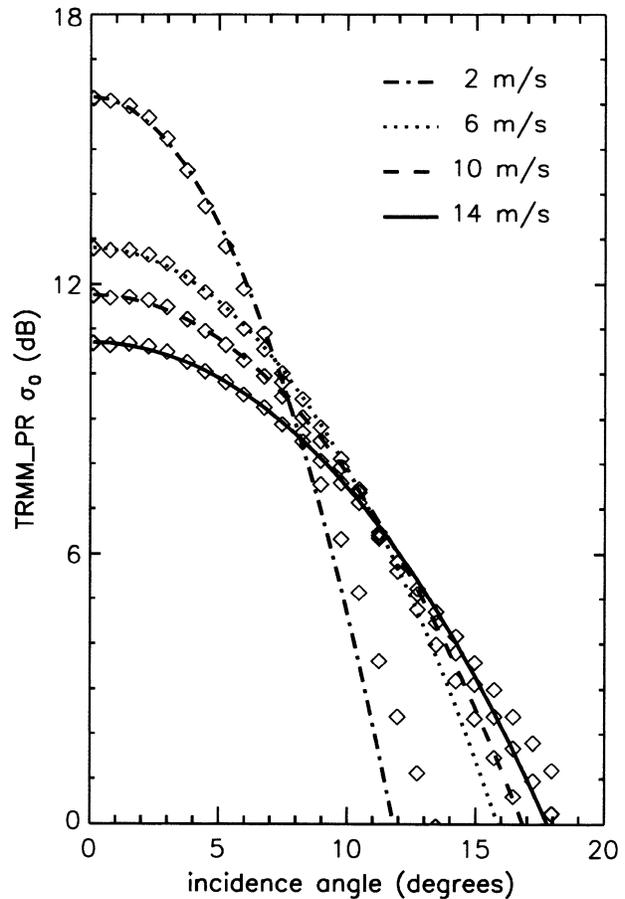

FIG. 5. PR model function values at selected wind speeds and incidence angles (diamonds) and least squares fits of (3) (solid lines).

values of effective nadir reflectivity and effective mean square slope can therefore be estimated at each wind speed by fitting (3) to the empirical model function at that wind speed over multiple incidence angles, assuming that $|R(0)|^2$ and $s(u)$ are not functions of θ. Importantly, the broad range of PR incidence angles allows solutions for both coefficients in (3) without prior specification of the wind speed dependence of either term.

Estimates of $|R(0)|^2$ and $s(u)$ were obtained at each wind speed from 0.20 m s^{-1} to 25 m s^{-1} (with 0.20 m s^{-1} resolution) from unweighted nonlinear least squares fits of (3) to the fully empirical PR model function across the entire range of PR incidence angles. (The fits were calculated using $\hat{\sigma}_0$ in natural, not dB, units.) The high quality of the fits at selected wind speeds is illustrated in Fig. 5, supporting the assumption that the coefficients $|R(0)|^2$ and $s(u)$ are independent of θ for small incidence angles. Owing to the rapid monotonic decrease of $\hat{\sigma}_0$ (at fixed wind speed) with θ, the least squares solutions disproportionately minimize deviations between the predictions of (3) and the model function at small incidence angles where $\hat{\sigma}_0$ is large. Indeed, the agreement between the empirical model functions

and the fits is excellent for $\theta \lesssim 10°$ at all wind speeds. This feature of the fits is actually beneficial for our analyses, since contributions to backscatter cross section from Bragg scattering (and concomitant unmeasured wind direction effects) increase at larger incidence angles. The results are negligibly changed when the fits are restricted to $0 \leq \theta \leq 10°$.

The near-convergence of the solution curves and the observations for $\theta \approx 11°$ are a manifestation of the relative insensitivity of σ_0 to wind speed for moderate to high wind speeds seen previously in Fig. 3. At higher incidence angles, the observations systematically exceed the fits. This is expected, since (3) neglects contributions to the backscatter from resonant (Bragg) mechanisms (Donelan and Pierson 1987; Plant 1990). The importance of this resonant scatter increases with increasing θ.

c. Effective nadir reflection coefficient [|R(0)|²]

Formulas for calculating the Fresnel reflection coefficient $|R(\theta)|^2$ can be found in many basic textbooks (e.g., Stewart 1985). They are applicable for partially conducting materials in the absence of surface roughness having wavelengths comparable to or smaller than the radar wavelength (i.e., effectively smooth surfaces). Using recent estimates for the complex reflectivity of the ocean at 14 GHz and realistic salinity and sea surface temperature from Apel (1994), the Fresnel reflection coefficient at $\theta = 0°$ has a value of 0.615. The reflectivity is only a weak function of θ; for comparison, $|R(18°)|^2 = 0.629$. For smooth surfaces, therefore, $|R(0)|^2$ should not vary with wind speed. However, since the smooth surface assumption is surely violated in the ocean, a wind speed dependence for the *effective* Ku-band reflection coefficient cannot be ruled out.

The best-fit solutions for $|R(0)|^2$ at each wind speed based on the PR data are shown in Fig. 6. The values of $|R(0)|^2$ vary between about 0.38 and 0.50 over the wind speed range 0–25 m s^{-1} (the variation is only between 0.45 and 0.50 for $1.5 \leq u \lesssim 15$ m s^{-1}). A mean value for $|R(0)|^2$ can be calculated by weighting the wind speed dependent $|R(0)|^2$ solutions by the observed collocated speed histogram (Fig. 2), yielding $|R(0)|^2 = 0.49$.

The interval corresponding to ± 1 standard deviation in the $|R(0)|^2$ estimates is also shown in Fig. 6. This uncertainty estimate is based solely on the residuals between the empirical model function value for mean cross section at each wind speed and incidence angle, and the best-fit prediction of (3), using the standard least squares assumptions (e.g., Press et al. 1996). For $u \lesssim 20$ m s^{-1}, the normalized uncertainty in $|R(0)|^2$ does not exceed 5% of the magnitude of the estimate.

Previous investigators analyzing Ku-band airborne and spaceborne altimeter data have argued that the effective Ku-band reflection coefficient must be significantly smaller than 0.62 in order to bring observed and
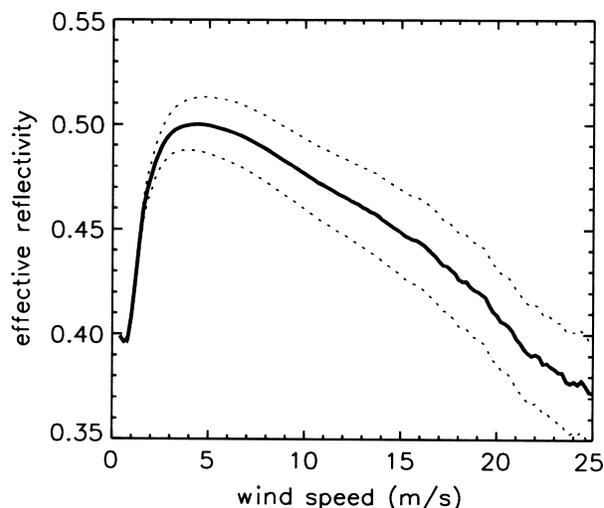

FIG. 6. Solid line: least squares solutions for $|R(0)|^2$ as a function of wind speed. Dotted lines: ± 1 standard deviation calculated from the two-parameter fit of the fully empirical model function to (3).

predicted cross sections into even approximate quantitative agreement. For example, Wu (1992) noted that the Brown (1979) altimeter model function (adjusted so that model cross sections were consistent with those from *Geosat* and TOPEX) required an effective reflection coefficient of 0.43; Jackson et al. (1992) found $|R(0)|^2 = 0.38$, and Apel (1994) suggested that $|R(0)|^2 = 0.34$.

The raw PR-based estimate is intermediate between the theoretical value for a smooth surface and the results of previous experimental investigations. The present result is surprisingly close to the value of 0.52 used by Schroeder et al. (1984) based on airborne RADSCAT data. However, as discussed in section 3b (Fig. 4), the PR nadir cross sections appear to be 1.92 dB larger than those from *Geosat* and TOPEX. If a multiplicative σ_0-matching approach such as that used by past investigators is applied to bring the nadir PR model function into conformance with *Geosat* and TOPEX observations, the weighted mean effective PR reflection coefficient would become $\sim 0.49/1.56 = 0.31$, about 8% and 18% smaller than the Apel (1994) and Jackson et al. (1992) values, respectively.

Small-scale surface roughness diffracts the incident radar pulse (Jackson et al. 1992, appendix B). Diffractive processes modify σ_0 in two ways of importance to this analysis. First, the diffractive contributions to σ_0 do not follow the incidence angle dependence predicted by (3). Second, diffraction reduces the effective quasi-specular reflection coefficient by a factor of $[1 - \beta^2 \langle h_s^2 \rangle]$ (Jackson et al. 1992), where $\langle h_s^2 \rangle$ is the spectrally integrated variance of small-scale roughness height (length scales shorter than some cutoff length on the order of the radar wavelength) and $\beta = 2k_{em} \cos\theta$ ($k_{em} = 289$ rad m^{-1} for the PR). Small-scale significant wave heights of ~ 1 mm are required to reduce effective re-

flection coefficients to the observed magnitudes. Enhanced wind speed dependencies of small-scale gravity-capillary and capillary waves (and hence $\langle h_s^2 \rangle$) could account for the observed wind speed dependence of $|R(0)|^2$.

We believe that the (presumably diffraction-induced) wind speed dependence of $|R(0)|^2$ shown in Fig. 6 for $u \gtrsim 3$ m s^{-1} is real. The observed 10% decrease has the same sign although it is nearly twice as large as that calculated by Jackson et al. (1992). On the other hand, the mild decrease in observed $|R(0)|^2$ for $2 \lesssim u \lesssim 3$ cannot easily be explained by diffractive effects. The larger decreases of $|R(0)|^2$ with decreasing u at very low winds may result from the TMI inaccuracies. If the TMI incorrectly underpredicts small wind speeds, then our empirical PR model function at low wind speed and low incidence angle will be biased low, which in turn would cause the $|R(0)|^2$ solutions to be biased low at these small wind speeds.

It is important to note that wind speed dependence of $|R(0)|^2$ cannot be determined empirically from analyses of nadir-looking radar altimeter data alone, since at nadir (3) becomes

$$\sigma_o(u; \theta = 0) = \frac{|R(0)|^2}{s(u)}. \tag{6}$$

Without a priori information regarding the wind speed dependence of effective mean square slope, it is impossible to use nadir σ_0 and wind speed measurements alone to separate wind speed dependencies of $|R(0)|^2$ from those of $s(u)$.

d. Effective mean square slope (s(u))

Estimates of $s(u)$ and standard errors from the least squares fits across incidence angles at fixed wind speeds are shown in Figs. 7a,b for the variable $|R(0)|^2$ calculated in the previous section. Figure 7a shows clearly that $s(u)$ is a nonlinear, monotonically increasing function of u for wind speeds below about 20 m s^{-1}.

There is no quantitative agreement in the literature about the wind speed dependence of (effective) mean square slope. Below we consider the empirical parameterization of Cox and Munk (1954) and the mixed dynamical/empirical parameterization of Wu (1972, 1990, 1992). In the next section, the modern wave model of Elfouhaily et al. (1997) is used to interpret the present PR results in terms of effective cutoff wavelength—the length scale of the shortest wave contributing to the effective mean square slope in (3).

The classical optical scattering data of Cox and Munk (1954) supported the hypothesis that mean square slope varied linearly with 10-m wind speed for both low-pass-filtered ("dirty") surfaces where only gravity waves were present, and for "clean" surfaces, which included capillary-wave-scale roughness. As shown by the dashed line in Fig. 7a, effective mean square slope inferred from the PR data is accurately parameterized by
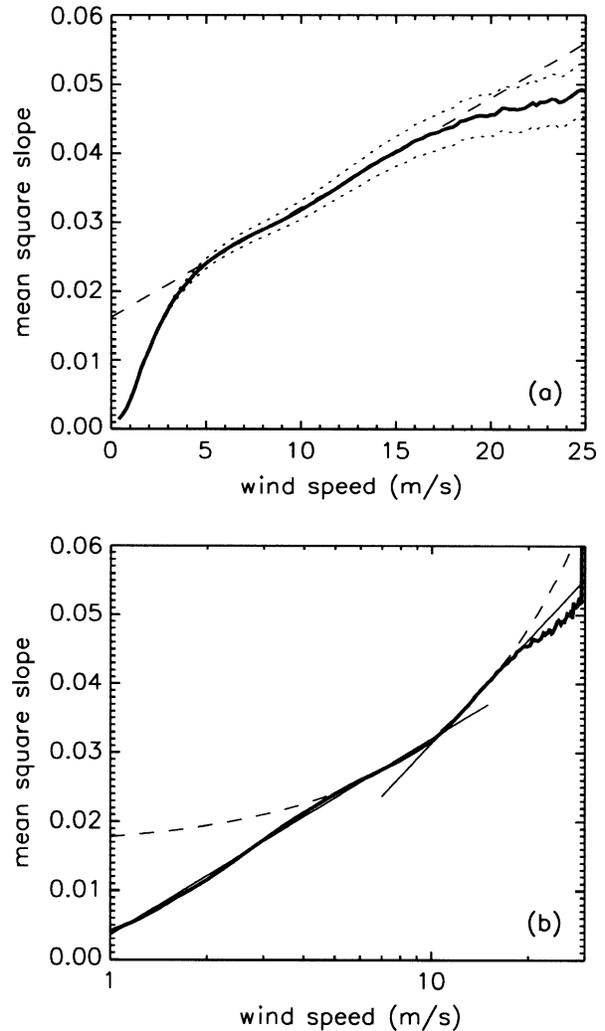

FIG. 7. Effective mean square slope [$s(u)$] from the two-parameter fit of the fully empirical model function to (3). (a) Solid line: least squares solution for $s(u)$. Dotted lines: ± 1 std dev. Dashed line: linear (Cox and Munk–type) parameterization based on a least squares fit for $5 \leq u \leq 15$ m s^{-1}. (b) As in (a), but with logarithmic abscissa. Light solid lines: best-fit two-branch logarithmic parameterization, with 10 m s^{-1} regime separation speed.

$$_{\text{lin}}s(u) = 0.016 + 0.0016u \tag{7}$$

for $u \geq 5$ m s^{-1}. This PR-based slope of 0.0016 is identical with the Cox and Munk (1954) result for a low-pass-filtered surface containing only gravity waves with wavelengths exceeding $\sim$0.3 m.

Wu (1972, 1990) replotted and edited the Cox and Munk results and suggested that mean square slope varied approximately with the logarithm of wind speed so that

$$_{\text{log}}s(u) = W_0 + W_1 \log_{10}u, \tag{8}$$

where W_0 and W_1 were empirically determined constants. Wu proposed that W_1 was constant (but different) in two regimes, defined generally by hydrodynamically

smooth flow at wind speeds below $\sim$7 m s^{-1} with a small wind speed sensitivity ($_{Wu}W_0 = 0.009$, $_{Wu}W_1 = 0.0276$), and hydrodynamically rough flow at higher wind speeds with a larger sensitivity $_{Wu}W_0 = -0.084$, $_{Wu}W_1 = 0.138$). The logarithmic wind speed dependence for $s(u)$ is clearly inapplicable at exceedingly low wind speeds for which $u \lesssim 10^{-(W_0/W_1)}$, where the parameterization predicts unphysical negative mean square slope.

The PR-based solution for $s(u)$ is replotted against $\log_{10}(u)$ in Fig. 7b. A dependence of $s(u)$ on $\log_{10}u$ is evident for $1 \le u \lesssim 10$ m s^{-1}. In this wind speed range, the PR data yield the coefficients $_{PR}W_0 = 0.0036$ and $_{PR}W_1 = 0.028$ (corresponding to a low wind speed cutoff of $\sim$0.75 m s^{-1}). The PR-based value of W_1 for low wind speeds is virtually identical to the value determined by Wu (1990). The constant term W_0 inferred from the PR data is about 44% of that derived by Wu (1990). Offsets of this magnitude are quantitatively consistent with the differences between the Cox and Munk clean versus dirty surface results, supporting the hypothesis that only roughness with length scales longer than that of the radar wavelength contribute to the observed backscatter cross section.

Both qualitative and quantitative approaches suggest that $_{PR}W_1$ changes abruptly near $\sim$10 m s^{-1}, in contradiction to the dynamically based reasoning of Wu (1972, 1990, 1992), which hypothesized that the transition would be located near 7 m s^{-1}. However, a slope change at 10 m s^{-1} is consistent with the early semiempirical nadir Ku-band model function of Brown (1979), which had a branch point at 9.2 m s^{-1}. The PR-based high wind speed sensitivity ($_{PR}W_1 = 0.050$) is only 36% of the Wu (1990) estimate ($_{Wu}W_1 = 0.138$ for $u \ge 7$ m s^{-1}). The discrepancy may be attributable to the fact that the effective cutoff wavelength for the Ku-band radar signal is intermediate between the clean and dirty surface cutoffs of the Cox and Munk dataset.

The accuracies of the parameterizations (7) and (8) are compared in Fig. 8. For $5 \lesssim u \lesssim 19$ m s^{-1}, both parameterizations are within about 2% (and typically much closer) of the $s(u)$ values inferred from the PR data. The logarithmic parameterization (8) is significantly more accurate than the linear parameterization (7) for $1 \le u \lesssim 5$ m s^{-1} (Figs. 7 and 8).

e. Cutoff wavenumber estimation

A longstanding open question critical to the proper physical interpretation of $s(u)$ in (3) relates to the magnitude of the cutoff wavelength, below which roughness contributes to diffractive scattering, and above which (3) accurately describes the observed scattering. Given a spectral wave model and accurate estimates of $s(u)$ from radar measurements, it is straightforward to integrate the model-predicted slope spectrum at each wind speed to determine the required cutoff wavelength or wavenumber. Inaccuracies in specification of $s(u)$ and/or errors in the wave model lead to errors in cutoff
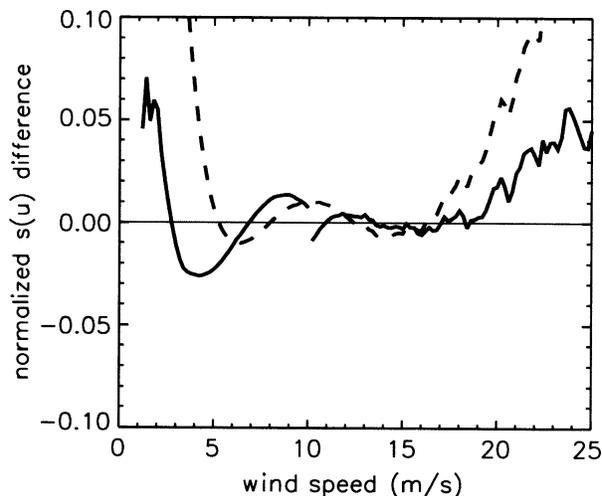

FIG. 8. Parameterization accuracies. Solid line: [$_{\log}s(u)/s(u) - 1$]. Dashed line: [$_{\lin}s(u)/s(u) - 1$].

wavelength estimates and inconsistencies between different investigations. For example, Thompson (1988) and Apel (1994) found that cutoff wavelength increased with increasing wind speed, while Wu (1972, 1990, 1992) concluded that cutoff wavelengths decreased with increasing wind speed, leading to apparently larger influence of the capillary wave portion of the spectrum on $s(u)$ at higher winds. Proper analysis of the data is further hindered when only nadir σ_0 measurements are used to specify $s(u)$ (or, equivalently, when $|R(0)|^2$ is assumed constant); in both cases, true wind speed variations of $|R(0)|^2$ cannot be determined and errors in cutoff wavelength estimates result.

The surprisingly robust linear Cox–Munk parameterization (7) and Wu's 2-branch logarithmic parameterization (8) have often been used to specify $s(u)$ in cutoff wavelength calculations. The Cox and Munk parameterization was based on limited optical scattering data with few measurements for $u \lesssim 5$ m s^{-1}. Its relevance to the issue of quasi-specular Ku-band radar scattering is uncertain, since the cutoff wavelength for the clean surface data for visible radiation must be much smaller than the centimeter radar wavelength, while the low-passed dirty surface suppressed roughness with wavelengths smaller than 30–40 cm (more than an order of magnitude longer than the Ku-band PR radar wavelength). The dynamical basis for the 2-branch logarithmic parameterization rested on limited contemporary understanding of the wind dependence, nonlinear transfers, and dissipative processes governing the high wavenumber, capillary portion of the surface wave spectrum.

Recent empirical and theoretical work has contributed to greatly improved spectral wave models. In this section, the modern wave model of Elfouhaily et al. (1997) is integrated and compared with the $s(u)$ inferred from the PR data to estimate effective Ku-band cutoff wavelengths for quasi-specular scattering.

Elfouhaily et al. (1997) reviewed recent surface wave models, and constructed a comprehensive spectral wave model (hereafter ECKV) that is consistent both with known dynamics and with a wide variety of high quality (nonradar) measurements. The model spans nearly 7 orders of magnitude in wavenumber and is supposed valid for wind speeds less than about 30 m s^{-1}.

The ECKV model accommodates fetch-limited conditions and predicts the two-dimensional surface elevation [$S(\mathbf{k})$] and curvature [$B(\mathbf{k}) = |\mathbf{k}|^3 S(\mathbf{k})$] spectra. For the present analyses, we typically assume fully developed seas throughout; although there are undoubtedly PR and TMI collocations obtained from fetch-limited conditions, the long duration of the dataset and the overwhelming preponderance of open ocean collocations assure that most measurements were obtained under fully developed conditions. Further, we assume that the wind directions corresponding to data at each wind speed were drawn from a uniform distribution (e.g., Wentz et al. 1984), and thus that the ECKV direction-averaged ("omni-directional") one-dimensional spectrum is applicable.

The derivation of the ECKV model is presented in detail in Elfouhaily et al. (1997). We calculate the filtered mean square slope from the ECKV omni-directional sea surface elevation spectrum by

$$s_E(u; k_c) \equiv \int_0^{k_c} k^2 S(k) \, dk, \qquad (9)$$

where s_E denotes a model estimate of (filtered) mean square slope, and k and k_c are the wavenumber and effective cutoff wavenumber magnitudes, respectively. A goal of the analysis is to determine k_c empirically by matching $s_E(u; k_c)$ with the $s(u)$ determined from the PR observations.

At high wavenumbers greater than about 10 times the wavenumber of the wind-speed-dependent peak of the sea surface elevation spectrum, the ECKV spectrum is highly dependent on friction velocity u_*. The TMI measurements provide no direct information on u_*, and thus it was necessary to infer u_* from the equivalent neutral stability 10-m TMI wind speed, which requires specification of the drag coefficient. For the purposes of this calculation, the parameterized polynomial form of the 10-m neutral drag coefficient developed by Taylor and Yelland (2001) was extended and used throughout the range $1.83 \leq u \leq 25$ m s^{-1}. For lower wind speeds down to 1 m s^{-1}, the smooth regime parameterization of Wu (1992) was used, leading to

$$C_{10} = [(1/\kappa) \ln(C_{10}^{1/2} uZ/\nu) + 5.5]^{-2},$$
$$\text{for } u < 1.83 \text{ m s}^{-1} \qquad (10a)$$
$$C_{10} = (0.87 + 0.0752u - 0.000661u^2) \times 10^{-3},$$
$$\text{for } u \geq 1.83 \text{ m s}^{-1}, \qquad (10b)$$

where $\kappa = 0.4$, $Z = 10$ m is the anemometer height,

and the kinematic viscosity of air was taken to be $\nu = 1.74 \times 10^{-5}$ m^2 s^{-1}.

The ECKV high wavenumber spectrum scales linearly with the Phillips/Kitaigorodskii equilibrium range parameter (denoted α_m). Elfouhaily et al. (1997) noted that α_m is not well constrained by existing measurements, especially at extreme low and high wind speeds. They proposed a two-regime logarithmic dependence for α_m that is somewhat consistent with recent measurements:

$$\alpha_m = 0.01[1 + \ln(u_*/c_m)] \qquad \text{for } u_* < c_m \quad (11a)$$
$$\alpha_m = 0.01[1 + 3\ln(u_*/c_m)] \quad \text{for } u_* \geq c_m, \quad (11b)$$

where $c_m = 0.23$ m s^{-1} corresponds to the capillary-gravity phase speed minimum. Unfortunately, (11a) yields unphysical negative α_m for $u_* \lesssim 0.085$ m s^{-1}, corresponding to $u \approx 3$ m s^{-1} according to (10). The Elfouhaily approximation also yields a noticeable slope discontinuity in the wind speed dependence of mean square slope near the hypothesized regime transition speed of ~ 7 m s^{-1}. However, Elfouhaily et al. (1997) show that (11b) is more accurate than their alternate linear parameterization:

$$\alpha_m = 0.014 \frac{u_*}{c_m}. \qquad (12)$$

In the present calculations, we have patched the logarithmic dependence of α_m on u_* for $u_* > 0.308$ m s^{-1} (11b) to the linear dependence of (12) for $u_* \leq 0.308$ m s^{-1} (which allows extension of the calculations to $u = 1$ m s^{-1}). For comparison, we have also used the two-branch logarithmic equilibrium parameterization proposed by Elfouhaily et al. (1997) and restricted the filtered mean square slope calculation to $u \gtrsim 3$ m s^{-1}.

The observed effective mean square slopes [$s(u)$] from section 4d are shown in Fig. 9a, plotted over predictions of the ECKV model (fully developed seas, patched linear/logarithmic dependence for α_m) for various ratios of cutoff to radar wavelengths (the PR wavelength is $\lambda_{em} = 2\pi/k_{em} = 2.16$ cm). The PR-based $s(u)$ solution corresponds to cutoff wavelengths (λ_c) between about 4 and 6 times longer than the radar wavelength for wind speeds between ~ 5 and 25 m s^{-1}, consistent with the airborne observations of Jackson et al. (1992).

Calculated values of λ_c are shown as a function of u in Fig. 9b for several combinations of inverse wave age and α_m parameterizations. For fully developed seas, the patched parameterization (11b) and (12) exhibits a smaller slope discontinuity for λ_c than does the two-branch logarithmic parameterization (11a,b). The calculation using the PR-based $s(u)$ and the ECKV model (assuming fully developed seas) yields cutoff wavelengths in the range $8.5 \lesssim \lambda_c \lesssim 13$ cm for wind speeds exceeding ~ 7 and ~ 5 m s^{-1} for the patched and two-branch logarithmic α_m parameterizations, respectively. Although the PR data are sparse for $u \gtrsim 20$ m s^{-1}, Fig. 9b shows no tendency for increasing λ_c with increasing
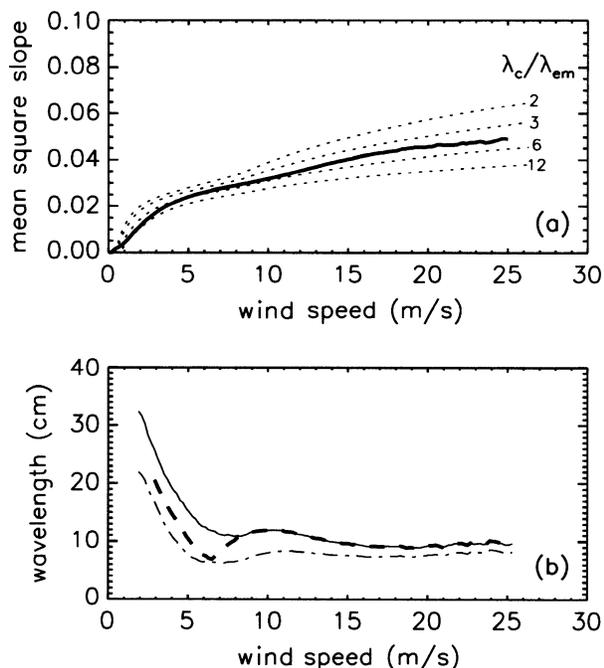
FIG. 9. (a) Effective mean square slopes calculated from PR data (solid line) and integrations of the ECKV slope spectrum for indicated λ_c/λ_{em} ratios (dotted lines). ECKV model predictions were based on the linear/logarithmic patched form for α_m (12, 11(b)) and assumed fully developed seas. (b) Cutoff wavelengths ($\lambda_c = 2\pi/k_c$) from (9). Solid line: patched linear–logarithmic α_m parameterization, fully developed seas. Dashed line: log–logα_m parameterization (12a,b) fully developed seas. Dash–dot line: patched linear–logα_m parameterization, underdeveloped conditions (wave age = 1).

FIG. 10. (a) Normalized sensitivity of λ_c to errors in $s(u)$. (b) Normalized expected errors in λ_c based on the sensitivities shown in (a) and the estimated $s(u)$ errors shown in Fig. 8a. Solid line: patched linear–logarithmic α_m parameterization, fully developed seas. Dotted line: patched linear–logarithmic α_m parameterization, underdeveloped conditions (wave age = 1).

u. The present analysis does not support the speculation by Wu (1972, 1990) that the fractional contributions of the gravity–capillary and capillary portions of the wave spectrum to air–sea momentum transfers increases with increasing wind speeds for $u \gtrsim 10$ m s^{-1}.

For wind speeds below about 5 m s^{-1}, the calculated cutoff wavelength increases rapidly with decreasing wind speed. The PR data analyzed in conjunction with the ECKV model suggests that the low wavenumber gravity wave field supports virtually the entire air–sea momentum transfer for these low wind speeds, consistent with the findings of Wu (1990) and the recent experimental results of Plant et al. (1999).

The calculation based on the assumption of slightly fetch-limited seas (wave age of 1.0) suggests that $\lambda_c \approx 8$ cm for $5 \lesssim u \lesssim 27$ m s^{-1} (dash–dot curve in Fig. 9b). As for the assumption of fully developed seas discussed above, λ_c increases rapidly with decreasing wind speed for $u \lesssim 5$ m s^{-1}.

Uncertainties in the calculated values of λ_c result from errors in the PR-based $s(u)$ solutions, scaled by the local wavenumber dependence of the integrand in (9). The normalized sensitivity $[\partial\lambda_c/\partial s_E(u; \lambda_c)]_{s(u)} s(u)/\hat{\lambda}_c$ [where $s(u)$ is the empirically determined effective mean square slope shown in Fig. 8 and $\hat{\lambda}_c$ is the solution of (9)] is shown in Fig. 10a for fully developed seas (solid line)
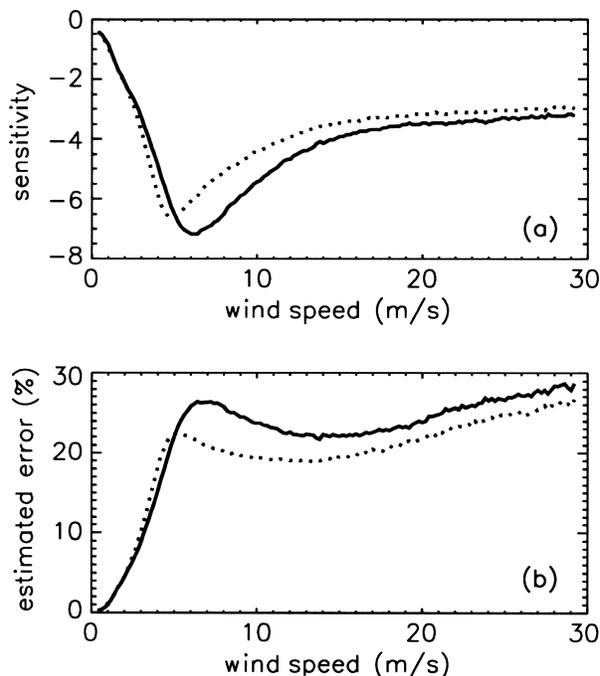
and for wave age = 1 (dotted line). Although for $u \gtrsim 15$ m s^{-1} a 1% increase in $s(u)$ results in a 4% decrease in λ_c, the sensitivity is significantly larger near the dynamical transition region $u \sim 6$–7 m s^{-1}. Multiplication of the normalized sensitivity (Fig. 10a) by the normalized $s(u)$ uncertainty (Fig. 8a) yields the total normalized uncertainty shown in Fig. 10b for both fully developed and slightly underdeveloped conditions. The 20%–25% uncertainties in λ_c correspond to dimensional uncertainties of only 2–3 cm.

5. Summary and conclusions

Wind speeds estimated by the passive TRMM Microwave Imager (TMI) and Ku-band (13.8 GHz) ocean surface backscatter cross sections (σ_0) measured simultaneously by the TRMM precipitation radar (PR) over the 1-yr period August 1999–July 2000 were collocated and used to construct fully empirical model functions at each incidence angle in the 215-km-wide PR swath. The model functions represent the first comprehensive quantitative description of the relationship between remotely sensed σ_0 and wind speed at small, but nonzero, incidence angles—the PR swath encompasses incidence angles from 0° to 18°. The nadir PR model function was compared with historical spaceborne altimeter measurements, and the complete set of multi-incidence angle model functions was used to elu-

cidate the magnitudes, wind speed dependencies, and interpretations of coefficients in the classical quasi-specular scattering theory for isotropic, Gaussian surfaces.

Except for a 1.9-dB bias, the nadir σ_0 dependence on wind speed derived from the collocated PR and TMI data was nearly identical with that found from the MCW (Witter and Chelton 1991) and Freilich and Challenor (1994) model functions that were based on TOPEX and *Geosat* measurements. The calibration difference may possibly result from differences in averaging approaches used in the low-level radar processing, coupled with a PR bias owing to the relatively wide range gates of weather radars in comparison with those of altimeters designed specifically to measure sea surface topography (Caylor et al. 1997).

The unique information in the collocated PR–TMI dataset results from the relatively wide range of incidence angles (θ) and wind conditions measured during the 1-yr data record analyzed here. By fitting the observed incidence angle dependence of the fully empirical PR model functions to quasi-specular scattering theory (3) at each wind speed, it was possible to solve directly and separately for the magnitudes and wind speed dependencies of the effective Ku-band nadir reflectivity [$|R(0)|^2$] and the effective Ku-band mean square slope (Figs. 6 and 7, respectively). After accounting for the overall 1.92-dB calibration difference, observed PR-based nadir reflectivities of $\sim$0.31 were comparable with (although 8%–18% smaller than) previous empirical estimates by others. In this first spaceborne confirmation of the aircraft-based findings of Jackson et al. (1992), the present analysis shows that $|R(0)|^2$ decreases with increasing wind speed for wind speeds u greater than 3.5 m s^{-1}. The data are consistent with the suggestion that large differences between the observed nadir ocean reflectivity and predictions based on laboratory measurements of dielectric properties result from wind speed dependent diffractive effects owing to small-scale roughness on the ocean surface.

Effective mean square slope [$s(u)$] varied monotonically but nonlinearly with 10-m wind speed. For $1 \lesssim u \lesssim 10$ m s^{-1}, the dependence of s on log$u$ (8) hypothesized by Wu (1990) was found to be quantitatively accurate. For $10 < u \lesssim 20$ m s^{-1}, the parameterization of s in terms of log$u$ was also accurate, although the slope from the PR-based calculation was only 30% of the Wu (1990) estimate (which included the effects of capillary wave-scale roughness). The 10 m s^{-1} transition wind speed found in the present analysis is higher than the value of 7 m s^{-1} suggested by Wu (1972) on dynamical grounds, but is consistent with the early results of Brown (1979), which were based on an extremely limited set of nadir altimeter measurements.

The linear dependence of mean square slope on u suggested by Cox and Munk (1954) was *also* found to be quantitatively accurate for $5 \lesssim u \lesssim 20$ m s^{-1}, with the PR-based slope (7) identical with the Cox and Munk result for a heavily low-pass-filtered surface. Over the wind speed range $5 \lesssim u \lesssim 19$ m s^{-1}, both the two-branch logarithmic parameterization and the linear parameterization of s on u were accurate to within $\sim$2% (and typically much better) of the measurements (Fig. 8). Thus, while the logarithmic parameterization is clearly more accurate at wind speeds from 1 to 5 m s^{-1}, the present data do not provide any basis for choosing between the two-branch logarithmic or linear parameterizations for higher winds.

The recent (ECKV) wave model of Elfouhaily et al. (1997) was used in conjunction with the PR-based $s(u)$ solutions to investigate the magnitude and wind speed dependence of the effective short wavelength cutoff (λ_c) for low incidence angle Ku-band scattering (Fig. 9). For $u \gtrsim 5$ m s^{-1}, the empirically determined λ_c (assuming fully developed seas) was found to be nearly constant and always within the range of about 4 to 6 times the radar wavelength (2.2 cm). This is consistent with the airborne results of Jackson et al. (1992) but in contrast with the findings of Donelan and Pierson (1987) and Apel (1994) whose wave models yield much larger (and wind speed dependent) cutoff wavelengths (not shown), and with the results of Wu (1972, 1990, 1992) who concluded that λ_c was strongly wind speed dependent at moderate to high wind speeds. For $u \lesssim 5$ m s^{-1}, the PR-based λ_c increases rapidly with decreasing u, consistent with the Wu (1990) and Plant et al. (1999) findings that long gravity waves support the entire air–sea momentum flux at low wind speeds.

The ECKV wave model was developed without reliance on radar data. Further, the assumptions inherent in the derivation of the quasi-specular scattering theory (2) and (3) require that the smallest effective cutoff wavelength be only a function of (and longer than) the radar wavelength, rather than having wind speed dependence (Brown 1990; Jackson et al. 1992). As suggested by the present analysis, wind speed dependence owing to diffractive effects from small-scale roughness elements will not obey the incidence angle dependence of (3), and will thus be manifested as wind speed dependent changes in $|R(0)|^2$, rather than s (or λ_c). The present results thus constitute a strong confirmation of the accuracy of the Elfouhaily et al. (1997) wave model, at least for fully developed sea conditions.

REFERENCES

Apel, J. R., 1994: An improved model of the ocean surface wave vector spectrum and its effects on radar backscatter. *J. Geophys. Res.,* **99,** 16 269–16 291.

Barrick, D. E., 1974: Wind dependence of quasi-specular microwave sea scatter. *IEEE Trans. Antennas Propag.,* **AP-22,** 135–136.

Brown, G. S., 1979: Estimation of surface wind speeds using satellite-borne radar measurements at normal incidence. *J. Geophys. Res.,* **84,** 3974–3978.

——, 1990: Quasi-specular scattering from the air–sea interface. *Surface Waves and Fluxes,* Vol. 2, W. Plant and G. Geerneart, Eds., Kluwer Academic, 1–40.

Caylor, I. J., G. M. Heysfield, R. Meneghini, and L. S. Miller, 1997: Correction of sampling errors in ocean surface cross-sectional estimates from nadir-looking weather radar. *J. Atmos. Oceanic Technol.,* **14,** 203–210.

Chelton, D. B., J. C. Ries, B. J. Haines, L.-L. Fu, and P. S. Callahan, 2001: Satellite altimetry. *Satellite Altimetry and Earth Sciences,* L.-L. Fu and A. Cazenave, Eds., Academic Press, 1–131.

Connor, L. N., and P. S. Chang, 2000: Ocean surface wind retrievals using the TRMM microwave imager. *IEEE Trans. Geosci. Remote Sens.,* **38,** 2009–2016.

Cox, C. S., and W. Munk, 1954: Statistics of the sea surface derived from sun glitter. *J. Mar. Res.,* **13,** 198–227.

Donelan, M., and W. J. Pierson, 1987: Radar scattering and equilibrium ranges in wind-generated waves with application to scatterometry. *J. Geophys. Res.,* **92,** 4971–5029.

Elfouhaily, T., B. Chapron, K. Katsaros, and D. Vandemark, 1997: A unified directional spectrum for long and short wind-driven waves. *J. Geophys. Res.,* **102,** 15 781–15 796.

Freilich, M. H., and R. S. Dunbar, 1993: Derivation of satellite wind model functions using operational surface wind analyses: An altimeter example. *J. Geophys. Res.,* **98,** 14 633–14 649.

——, and P. G. Challenor, 1994: A new approach for determining fully empirical altimeter wind speed model functions. *J. Geophys. Res.,* **99,** 25 051–25 062.

Grantham, W. L., E. M. Bracalante, W. L. Jones, and J. W. Johnson, 1977: The Seasat—A satellite scatterometer. *IEEE J. Oceanic Eng.,* **OE-2,** 200–206.

Holliday, D., G. St.-Cyr, and N. E. Woods, 1986: A radar ocean imaging model for small to moderate incidence angles. *Int. J. Remote Sens.,* **7,** 1809–1834.

Jackson, F. C., W. T. Walton, and D. E. Hines, 1992: Sea surface mean square slope from Ku-band backscatter data. *J. Geophys. Res.,* **97,** 11 411–11 427.

Kozu, T., and Coauthors, 2001: Development of precipitation radar onboard the Tropical Rainfall Measuring Mission (TRMM) satellite. *IEEE Trans. Geosci. Remote Sens.,* **39,** 102–116.

Kummerow, C., W. Barnes, T. Kozu, J. Shiue, and J. Simpson, 1998: The Tropical Rainfall Measuring Mission (TRMM) sensor package. *J. Atmos. Oceanic Technol.,* **15,** 809–817.

——, and Coauthors, 2000: The status of the Tropical Rainfall Measuring Mission (TRMM) after two years in orbit. *J. Appl. Meteor.,* **39,** 1965–1982.

Li, L., E. Im, S. L. Durden, and Z. S. Haddad, 2002: A surface wind model-based method to estimate path-induced radar path attenuation over ocean. *J. Atmos. Oceanic Technol.,* **19,** 658–672.

Mears, C. A., D. K. Smith, and F. J. Wentz, 2001: Comparison of SSM/I and buoy-measured wind speeds from 1987 to 1997. *J. Geophys. Res.,* **106,** 11 719–11 729.

Meissner, T., D. Smith, and F. J. Wentz, 2001: A 10 year intercomparison between collocated Special Sensor Microwave Imager oceanic surface wind speed retrievals and global analyses. *J. Geophys. Res.,* **106,** 11 731–11 742.

Meneghini, R., T. Iguchi, T. Kozu, L. Liao, K. Okamoto, J. A. Jones, and J. Kwiatowski, 2000: Use of the surface reference technique for path attenuation estimates from the TRMM precipitation radar. *J. Appl. Meteor.,* **39,** 2053–2070.

Naderi, F. M., M. H. Freilich, and D. G. Long, 1991: Spaceborne radar measurement of wind velocity over the ocean—An overview of the NSCAT scatterometer system. *Proc. IEEE,* **79,** 850–866.

Plant, W. J., 1990: Bragg scattering of electromagnetic waves from the air/sea interface. *Surface Waves and Fluxes,* Vol. 2, W. Plant and G. Geerneart, Eds., Kluwer Academic, 41–108.

——, D. E. Weissman, W. C. Keller, V. Hessany, K. Hayes, and K. W. Hoppe, 1999: Air/sea momentum transfer and the microwave cross section of the sea. *J. Geophys. Res.,* **104,** 11 173–11 191.

Press, W. H., S. A. Teukolsky, W. T. Vetterling, and B. P. Flannery, 1996: *Numerical Recipes in Fortran 77.* Vol. 1. 2d ed. Cambridge University Press, 933 pp.

Schroeder, L. C., W. L. Jones, P. R. Schaffner, and J. L. Mitchell, 1984: Flight measurements and analysis of AAFE RADSCAT wind speed signature of the ocean. NASA Tech. Memo. 85646, 144 pp.

Stewart, R. H., 1985: *Methods of Satellite Oceanography.* University of California Press, 360 pp.

Stoffelen, A., and D. L. T. Anderson, 1997: Scatterometer data interpretation: Derivation of the transfer function CMOD4. *J. Geophys. Res.,* **102,** 5767–5780.

Taylor, P. K., and M. J. Yelland, 2001: The dependence of sea surface roughness on the height and steepness of the waves. *J. Phys. Oceanogr.,* **31,** 572–590.

Thompson, D. R., 1988: Calculation of radar backscatter modulations from internal waves. *J. Geophys. Res.,* **93,** 12 371–12 380.

Valenzuela, G. R., 1978: Theories for the interaction of electromagnetic and oceanic waves—A review. *Bound.-Layer Meteor.,* **13,** 61–85.

Wentz, F. J., 1997: A well calibrated ocean algorithm for special sensor microwave/imager. *J. Geophys. Res.,* **102,** 8703–8718.

——, and R. W. Spencer, 1998: SSM/I rain retrievals within a unified all-weather ocean algorithm. *J. Atmos. Sci.,* **55,** 1613–1627.

——, and D. K. Smith, 1999: A model function for the ocean-normalized radar cross section at 14 GHz derived from NSCAT observations. *J. Geophys. Res.,* **104,** 11 499–11 514.

——, S. Peteherych, and L. A. Thomas, 1984: A model function for ocean radar cross-sections at 14.6 GHz. *J. Geophys. Res.,* **89,** 3689–3704.

——, P. D. Ashcroft, and C. L. Gentemann, 2001: Post-launch calibration of the TMI microwave radiometer. *IEEE Trans. Geosci. Remote Sens.,* **39,** 415–422.

Witter, D. L., and D. B. Chelton, 1991: A GEOSAT wind speed algorithm and a method for altimeter wind speed algorithm development. *J. Geophys. Res.,* **96,** 8853–8860.

Wu, J., 1972: Sea-surface slope and equilibrium wind-wave spectra. *Phys. Fluids,* **15,** 741–747.

——, 1990: Mean square slopes of the wind-disturbed water surface, their magnitude, directionality, and composition. *Radio Sci.,* **25,** 37–48.

——, 1992: Near-nadir microwave specular returns from the sea surface—Altimeter algorithms for wind and wind stress. *J. Atmos. Oceanic Technol.,* **9,** 659–667.